

• Article •

SPECIAL TOPIC:

xxx 2020 Vol. xx No. x: 000000
<https://doi.org/xx>

The clustering of galaxies in the DESI imaging legacy surveys DR8: I. the luminosity and color dependent intrinsic clustering

Zhaoyu Wang ¹, Haojie Xu ¹, Xiaohu Yang ^{1,2*}, Yipeng Jing ^{1,2*}, Kai Wang ^{3,4}, Hong Guo ⁵,
 Fuyu Dong ⁶, and Min He ¹

¹*Department of Astronomy, School of Physics and Astronomy, and Shanghai Key Laboratory for Particle Physics and Cosmology,
 Shanghai Jiao Tong University, Shanghai 200240, China;*

²*Tsung-Dao Lee Institute and Key Laboratory for Particle Physics, Astrophysics and Cosmology, Ministry of Education,
 Shanghai Jiao Tong University, Shanghai 200240, China;*

³*Department of Astronomy, Tsinghua University, Beijing 100084, China;*

⁴*Department of Astronomy, University of Massachusetts Amherst, MA 01003, USA;*

⁵*Key Laboratory for Research in Galaxies and Cosmology, Shanghai Astronomical Observatory, Shanghai 200030, China;*

⁶*School of Physics, Korea Institute for Advanced Study (KIAS), 85 Hoegiro, Dongdaemun-gu, Seoul, 02455, Republic of Korea*

Received xxx xxx, 2020; accepted xxx xxx, 2020

In a recent study, we developed a method to model the impact of photometric redshift uncertainty on the two-point correlation function (2PCF). In this method, we can obtain both the intrinsic clustering strength and the photometric redshift errors simultaneously by fitting the projected 2PCF with two integration depths along the line-of-sight. Here we apply this method to the DESI Legacy Imaging Surveys Data Release 8 (LS DR8), the largest galaxy sample currently available. We separate galaxies into 20 samples in 8 redshift bins from $z = 0.1$ to $z = 1.0$, and a few z-band absolute magnitude bins, with $M_z \leq -20$. These galaxies are further separated into red and blue sub-samples according to their $M_r^{0.5} - M_z^{0.5}$ colors. We measure the projected 2PCFs for all these galaxy (sub-)samples, and fit them using our photometric redshift 2PCF model. We find that the photometric redshift errors are smaller in red sub-samples than the overall population. On the other hand, there might be some systematic photometric redshift errors in the blue sub-samples, so that some of the sub-samples show significantly enhanced 2PCF at large scales. Therefore, focusing only on the red and all (sub-)samples, we find that the biases of galaxies in these (sub-)samples show clear color, redshift and luminosity dependencies, in that red brighter galaxies at higher redshift are more biased than their bluer and low redshift counterparts. Apart from the best fit set of parameters, σ_z and b , from this state-of-the-art photometric redshift survey, we obtain high precision intrinsic clustering measurements for these 40 red and all galaxy (sub-)samples. These measurements on large and small scales hold important information regarding the cosmology and galaxy formation, which will be used in our subsequent probes in this series.

dark matter, large-scale structure, cosmology

PACS number(s): 95.35.+d, 98.65.r, 98.80.k

Citation: Wang, Z., Xu, H., Yang, X. et al., The clustering of galaxies in the DESI imaging legacy surveys DR8: I. the luminosity and color dependent intrinsic clustering, *Sci. China-Phys. Mech. Astron.* **xx**, 000000 (2020), <https://doi.org/xx>

1 Introduction

Past decades have seen the flourishing of large galaxy redshift surveys. A large number of surveys, such

as the Las Campanas Redshift Survey (LCRS) [1], the 2 degree Field Galaxy Redshift Survey (2dFGRS) [2],

*Corresponding authors (Xiaohu Yang, email: xyang@sjtu.edu.cn; Yipeng Jing, email: yjing@sjtu.edu.cn)

the Sloan Digital Sky Survey (SDSS) [3], the DEEP2 Galaxy Redshift Survey (DEEP2) [4, 5], and the VIMOS Public Extragalactic Redshift Survey (VIPERS) [6] have provided tremendous measurements of the galaxy spatial distributions, which enable us to explore precise cosmological parameters. The Baryon Acoustic Oscillations (BAO) [7-11], gravitational lensing [12-20], power spectrum [21-29] and correlation functions (such as two-point correlation functions (2PCF) and three-point correlation functions (3PCF) [30-32] are often used to depict the universe.

The 2PCF, a second-order moment statistics, or its integrated version, the projected 2PCF, are usually employed to characterize the clustering strength of galaxies. Numerous studies with galaxy samples at low- z and intermediate- z reveal strong correlations between clustering strength and galaxy properties, such as color, luminosity, spectral type [33-43] and so on.

To explain the correlation between clustering strength and galaxy properties, some statistical model based on halo-galaxy connection are proposed, such as the halo occupation distribution (HOD) [33, 38, 42, 44-50], the conditional luminosity function model (CLF) [51-55] and halo abundance matching [46, 56]. These models transform galaxy clustering measurements to the informative, physical relation between galaxies and dark matter halos, which encodes the complex physics of galaxy formation and evolution, and are very helpful in diagnosing galaxy formation theories. Under the HOD/CLF framework, tight constraints on the cosmology can also be achieved by a combination of galaxy clustering, dynamical clustering measurements (i.e., pairwise radial velocity dispersion of galaxies), and galaxy-galaxy lensing [59-61].

Most of the previous work on galaxy clustering focus on galaxies with spectroscopic redshift (spec_z), which is relatively easy to measure in local universe. For high- z galaxies, due to the observational limitation and measurement difficulty, one can only get a relatively small galaxy sample in a small volume, such as DEEP2 [4, 5], zCOSMOS [62]. Hence, the 2PCF measurement will become noisy due to the Poisson noise and cosmic variance, especially on large scales.

In general, there are two types of approaches to infer galaxy-halo connection at these high redshifts to increase the signal-to-noise ratios of the clustering measurements. One is to measure the cross-correlation between the photometric and spectroscopic samples [63-66] and the other is to directly model the angular galaxy clustering measurements [67-70, 100]. However, both approaches have their own limitations. The cross-correlation method is limited by the size of

the spectroscopic sample and needs careful treatment of the interlopers, while the galaxy-halo connection in the angular clustering method is less well constrained due to the lack of redshift information and hard to probe the redshift evolution of galaxies.

To overcome these problems, we proposed a new method in [71] (hereafter W19) to directly measure the projected 2PCFs from galaxies with only photometric redshifts. In W19, we constructed a realistic mock light-cone from N-body simulation where the galaxies are populated using HOD model. The tests showed that our method can not only recover the 2PCF, but also constrain the photometric redshift uncertainties, which is not achievable for previous methods [66, 68, 72].

In this paper, we will apply the method developed in W19 to the DESI Legacy Imaging Surveys. Here we aim to obtain the intrinsic (i.e. corrected for the impact of photometric redshift errors) projected 2PCFs for sets of galaxy (sub-)samples in different luminosity and redshift bins. In this regards, before the availability of the spectroscopic redshifts from the subsequent DESI observations, we can already have clustering measurements that are much accurate than before for the current galaxy formation and cosmological studies. The structure of this paper is organized as follows. First, we introduce the DESI Legacy Imaging Surveys data and our clustering measurement method in §2. Then photometric redshift modeling of the 2PCF is presented in §3. We show the main results in §4 and the summary in §5. Throughout this paper, we assume a Λ CDM cosmology that are consistent with the Planck 2018 results [73]: $\Omega_m = 0.315$, $\Omega_\Lambda = 0.685$, $n_s = 0.965$, $h = H_0/(100 \text{ km s}^{-1} \text{ Mpc}^{-1}) = 0.674$ and $\sigma_8 = 0.811$.

2 Galaxy Samples and Clustering Measurements

We investigate the luminosity and color dependence of intrinsic galaxy clustering with the DESI Legacy Imaging Surveys Date Release 8 (LS DR8; [76]). LS DR8 provides target catalogs for The Dark Energy Spectroscopic Instrument (DESI; [75]), the next generation spectroscopic survey for measuring the dark energy effect on the expansion of the universe. All the galaxy positions and properties are extracted from here¹⁾.

Following the target selection criteria lay out in Yang et al. (2020) [74], we select out galaxies by morphological classification as type *REX*, *EXP*, *DEV*, and *COMP* from TRAC-TOR [77] fitting results²⁾. We also remove those objects at

1) <https://www.legacysurvey.org/dr8/files/>

2) In the Tractor fitting procedure, *REX* stands for round exponential galaxies with a variable radius, *DEV* for deVaucouleurs profiles (elliptical galaxies), *EXP* for exponential profiles (spiral galaxies), and *COMP* for composite profiles that are deVaucouleurs plus exponential (with the same source center).

low galactic latitudes and in the vicinity of masked pixels and bright stars (see the selection details in section 2.1 [74]).

The corresponding photometric redshift (photoz hereafter) catalog is adopted from the Photometric Redshifts for the Legacy Surveys (PRLS³⁾[81]), who employs random forest algorithm [84] to estimate the photoz. Same as the procedures done in [74], we select galaxies with $z \leq 21$ and $0 < z_{\text{phot_median}} \leq 1$, where the $z_{\text{phot_median}}$ is the median value of photoz probability distribution function. For those provided with spectroscopic redshift⁴⁾ in the catalog, we replace the photometric redshift with the spectroscopic redshift. We include also additional spectroscopic redshifts matching from the 2MASS Redshift Survey (2MRS [85]), 6dF Galaxy Survey Data Release 3 (6dFGRS [86]), and 2dF Galaxy Redshift Survey (2dFGRS [2]).

All the magnitudes and color used in the work are in the AB system and corrected for Galactic extinction. We convert apparent magnitude to absolute magnitude via the following equation,

$$M_x - 5 \log h = m_x - DM(z) - K_x^{0.5}$$

where $x \equiv r, z$ and $DM(z)$ is the distance module corresponding to redshift z ,

$$DM(z) = 5 \log D_L(z) + 25$$

with $D_L(z)$ being the luminosity distance in h^{-1}Mpc . $K_x^{0.5}$ represents the K-correction in x-band to sample median redshift $z \sim 0.5$. Here K-correction is obtained for each galaxy according to its three optical (grz) bands, two mid-infrared (W1 $3.4\mu\text{m}$, W2 $4.6\mu\text{m}$) bands photometries and the photoz information using the ‘Kcorrect’ model (eg. v4_3) described in [87]. Those who are interested can refer to [74] to see an illustration of the z -band K-correction distributions as a function of redshift in their Fig. 2. In general, the photoz error can impact both the K-correction as well as the luminosity distance measurements, and hence the absolute magnitude estimation. However, since the overall quality of the photoz estimation in [81] is remarkably good, the distance error in general is smaller than 5%. We neglect its impact on the absolute magnitude estimation for each galaxy.

2.1 Galaxy Sample Construction with Luminosity, Redshift, and Color

To investigate first the luminosity dependence of intrinsic galaxy clustering and photoz errors, we construct galaxy samples in bins of redshift and galaxy luminosity, in light of the

fact that both galaxy bias and photoz quality are primarily dependent on galaxy luminosity and redshift. Zhou et al.[81] suggested that galaxy photoz overall are most accurate with $z < 21$ (see their Appendix B for details), we therefore adopt the z band absolute magnitude ($M_z^{0.5} - 5 \log h$) as our galaxy luminosity indicator. Since the photoz error is much larger than specz error, a relatively large redshift bin ($\Delta z = 0.2$ in this work) for galaxy samples is preferred to mitigate the effect due to galaxy interlopers from neighboring redshift bins. In principle, we divide the galaxies with absolute magnitude bin width $\Delta(M_z^{0.5} - 5 \log h) = 1$ mag, but the enormous amount of galaxies in some galaxy samples (more than 20 million galaxies) allows us to probe more subtle luminosity dependence. For this reason, in those samples we further divide galaxies into bin with $\Delta(M_z^{0.5} - 5 \log h) = 0.5$ mag, regardless of galaxy number counts in these samples afterwards.

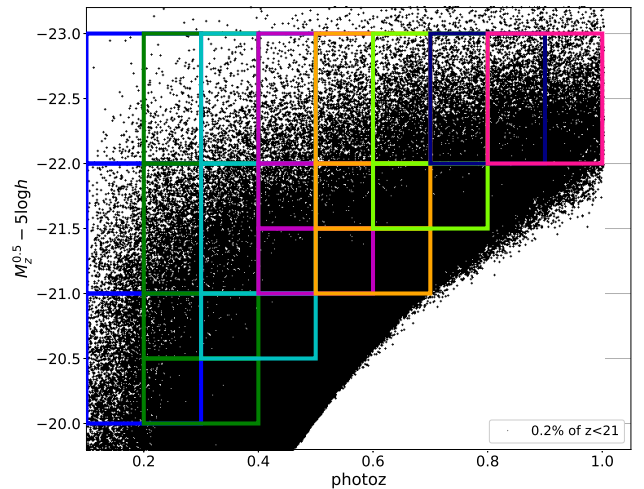


Figure 1 Construction of galaxy samples in bins of $M_z^{0.5} - 5 \log h$ and photoz. Each patch represents a luminosity volume-limit sample, with different color corresponding to different redshift bin. All luminosity samples span redshift with $\Delta z = 0.2$ and the artificial $z \leq 21$ flux limit we choose determines how faint we construct the samples. As discussed in section 2.1, some luminosity bins have absolute magnitude bin width $\Delta(M_z^{0.5} - 5 \log h) = 0.5$ mag, depending on the galaxy numbers. The maximum luminosity goes to $M_z^{0.5} - 5 \log h = -23$ for all redshift bins. To avoid saturation, here we only plot the distribution of randomly selected 0.2% galaxies.

With the above consideration taken into account, the redshift of the galaxy samples ranges from centering at $z = 0.2$ to at $z = 0.9$, the galaxy samples are constructed in a volume-limited way. We end up with 20 galaxy samples defined by bins in $M_z^{0.5} - 5 \log h$ and photoz and covering the galaxy luminosity-redshift diagram, which is shown in Fig. 1. More detailed galaxy sample information is summarized in Table

3) <https://www.legacysurvey.org/dr8/files/#photometric-redshift-files-8-0-photo-z-sweep-brickmin-brickmax-pz-fits>

4) The spectroscopic redshifts are from BOSS, SDSS, WiggleZ, GAMA, COSMOS2015, VIPERS, eBOSS, DEEP2, AGES, 2dFLenS, VVDS, and OzDES. See details in section 3.2 [81]

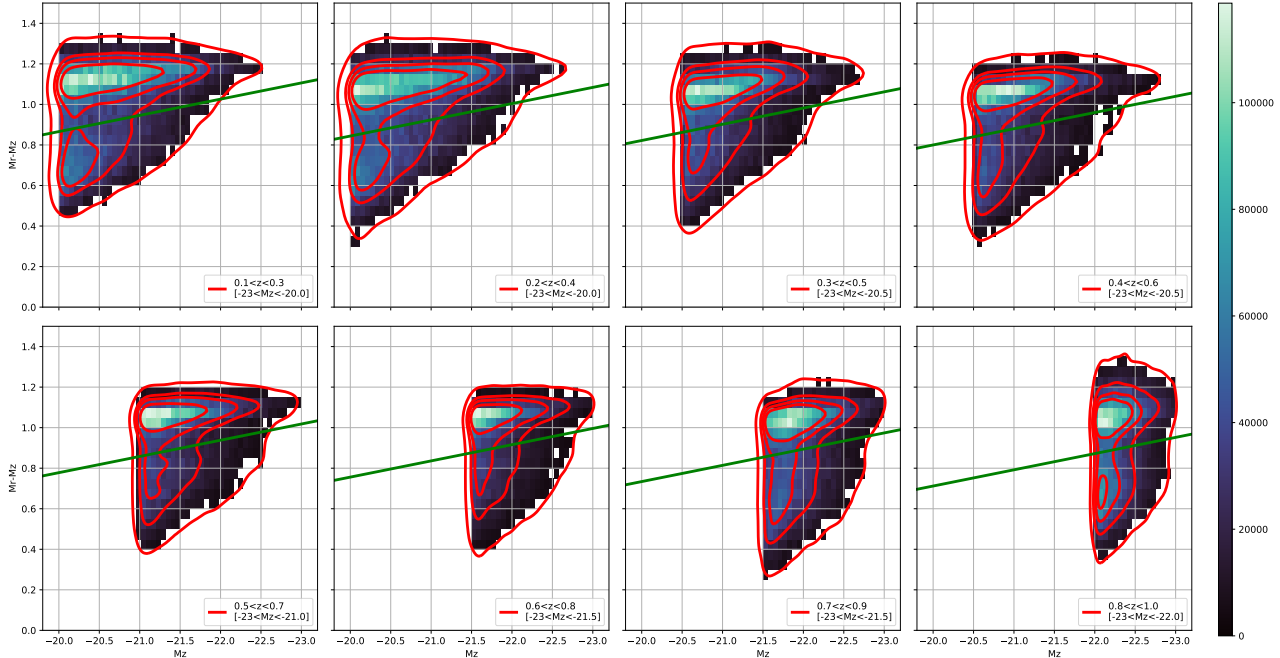


Figure 2 K-corrected $M_r^{0.5} - M_z^{0.5}$ vs. $M_z^{0.5} - 5 \log h$ for a random subsample (50,000 galaxies in each panel) of volume-limited luminosity samples as a function of redshift. The 2D histogram in each panel shows galaxy number counts in fine bins of color and magnitude, where color codes the galaxy number counts per magnitude per color, i.e., $d^2N_g/d(M_z^{0.5} - 5 \log h)/d(M_r^{0.5} - M_z^{0.5})$. The contours gives a less cluttered view of the 2D histogram. The green solid line (Eq.1) divides the luminosity samples into red/blue (or passive/star-forming) subsamples, taking into account of the dependence on luminosity and redshift. Note that M_z shown in the legends refers to $M_z^{0.5} - 5 \log h$.

1.

In addition to luminosity and redshift, galaxy clustering depends also on color, spectra type, morphology and surface brightness [36, 38, 43, 82]. These properties are strongly correlated with each other and display a similar change of clustering when dividing galaxies based on them [82]. In this work, we choose color since it is the immediately available quantity and the least vulnerable one to measurement uncertainties. Besides this, Blanton [83] found that luminosity and color are the two most predictive quantities for the galaxy local density, with weak residual dependence on morphology or surface brightness once the luminosity and color is fixed.

Following the color division practice at low redshift universe, we plot the color-magnitude diagram constructed from a random down-sampling (50,000) of previous volume-limited luminosity samples as a function of redshift, shown in Fig. 2. The contours demonstrate two galaxy populations with a tight red sequence and a lose blue cloud in all redshift, which allows us to divide the galaxy into red/blue (or passive/star-forming) subsamples by the following equation,

$$M_r^{0.5} - M_z^{0.5} = -0.8 - 0.08 * (M_z^{0.5} - 5 \log h) - 0.22 * (z - 0.5) \quad (1)$$

where the $M_r^{0.5} - M_z^{0.5}$ is the r-band absolute magnitude. It seems that $M_r^{0.5} - M_z^{0.5}$ color serves well for the passive/star-forming subsamples division. It might due to the fact that

the 4000Å break moves to r-band at $z \sim 0.5$, where the K-correction is performed. Note that at relatively high redshift, the dust could play a big role in linking the color and star-forming activity such that star-forming galaxies may exhibit a red color. To what extend this effect could contaminate our color subsamples needs a further study and it exceeds the scope of this work.

2.2 Galaxy Clustering Measurements

In W19, we demonstrated that intrinsic clustering and photoz uncertainty can be simultaneously constrained using the projected 2PCF. In this work we measure the projected 2PCF through the following equation,

$$w_p^{\text{obs}}(r_p | r_{\pi, \text{max}}) = 2 \int_0^{r_{\pi, \text{max}}} \xi^{\text{obs}}(r_p, r_{\pi}) dr_{\pi}. \quad (2)$$

where r_p and r_{π} are the transverse and line-of-sight separation between galaxy pair, $r_{\pi, \text{max}}$ is the upper bound of the integration along the line-of-sight direction. Since the methodology requires to measure the projected 2PCF with two different $r_{\pi, \text{max}}$, we choose $r_{\pi, \text{max}} = 50$ and $100 h^{-1} \text{Mpc}$ in this work for w_p measurements for all the galaxy (sub-)samples. ξ^{obs} is the two-dimensional correlation function in redshift space. We estimate $\xi^{\text{obs}}(r_p, r_{\pi})$ using the Landy-Szalay esti-

Table 1 The (sub-)samples selection criteria, number, number density, the related σ_z and galaxy bias best fitting results for all and red galaxies.

Sample	redshift	absolute magnitude	numbers (all/red)	number density (all/red)	σ_z (all/red)	bias (all/red)
$M_z^{0.5} - 5 \log h$						
				$10^{-4} (h^{-1} \text{Mpc})^{-3}$		
1	[0.1,0.3]	[-21.0,-20.0]	6636956/4162406	64.6715/40.5591	$0.0149^{+0.0005}_{-0.0004}/0.0134^{+0.0004}_{-0.0003}$	$1.0591^{+0.0114}_{-0.0107}/1.2402^{+0.0103}_{-0.0099}$
2	[0.1,0.3]	[-22.0,-21.0]	2502266/1908969	24.3824/18.6013	$0.0110^{+0.0002}_{-0.0002}/0.0103^{+0.0002}_{-0.0002}$	$1.2065^{+0.0066}_{-0.0064}/1.3202^{+0.0067}_{-0.0065}$
3	[0.1,0.3]	[-23.0,-22.0]	264990/226065	2.5821/2.2028	$0.0076^{+0.0002}_{-0.0002}/0.0069^{+0.0003}_{-0.0003}$	$1.6373^{+0.0091}_{-0.0092}/1.7131^{+0.0096}_{-0.0097}$
4	[0.2,0.4]	[-20.5,-20.0]	7648188/4408031	38.2338/22.036	$0.0242^{+0.0020}_{-0.0016}/0.0201^{+0.0010}_{-0.0008}$	$1.1045^{+0.0375}_{-0.0313}/1.2765^{+0.0249}_{-0.0217}$
5	[0.2,0.4]	[-21.0,-20.5]	5322863/3526769	26.6093/17.6305	$0.0197^{+0.0009}_{-0.0008}/0.0178^{+0.0007}_{-0.0006}$	$1.1771^{+0.0220}_{-0.0198}/1.3297^{+0.0188}_{-0.0173}$
6	[0.2,0.4]	[-22.0,-21.0]	5070090/3850127	25.3457/19.247	$0.0151^{+0.0004}_{-0.0003}/0.0140^{+0.0003}_{-0.0003}$	$1.2914^{+0.0109}_{-0.0103}/1.4010^{+0.0104}_{-0.0099}$
7	[0.2,0.4]	[-23.0,-22.0]	610255/531282	3.0507/2.6559	$0.0087^{+0.0002}_{-0.0002}/0.0080^{+0.0002}_{-0.0002}$	$1.6975^{+0.0080}_{-0.0079}/1.7701^{+0.0070}_{-0.0070}$
8	[0.3,0.5]	[-21.0,-20.5]	9482610/5793204	30.1603/18.4258	$0.0265^{+0.0025}_{-0.0019}/0.0223^{+0.0012}_{-0.0011}$	$1.2572^{+0.0505}_{-0.0406}/1.3740^{+0.0318}_{-0.0278}$
9	[0.3,0.5]	[-22.0,-21.0]	8633198/6279861	27.4587/19.9737	$0.0190^{+0.0006}_{-0.0006}/0.0172^{+0.0005}_{-0.0005}$	$1.3494^{+0.0180}_{-0.0167}/1.4553^{+0.0157}_{-0.0146}$
10	[0.3,0.5]	[-23.0,-22.0]	1082075/899869	3.4416/2.8621	$0.0099^{+0.0002}_{-0.0002}/0.0090^{+0.0002}_{-0.0002}$	$1.7283^{+0.0076}_{-0.0073}/1.8351^{+0.0075}_{-0.0073}$
11	[0.4,0.6]	[-21.5,-21.0]	8313880/5541092	19.0616/12.7043	$0.0213^{+0.0010}_{-0.0009}/0.0194^{+0.0007}_{-0.0006}$	$1.3579^{+0.0268}_{-0.0239}/1.4873^{+0.0209}_{-0.0198}$
12	[0.4,0.6]	[-22.0,-21.5]	3796681/2715952	8.7048/6.2270	$0.0158^{+0.0004}_{-0.0004}/0.0147^{+0.0003}_{-0.0003}$	$1.4767^{+0.0130}_{-0.0120}/1.6258^{+0.0129}_{-0.0121}$
13	[0.4,0.6]	[-23.0,-22.0]	1813560/1355864	4.1580/3.1087	$0.0099^{+0.0002}_{-0.0002}/0.0089^{+0.0002}_{-0.0002}$	$1.7552^{+0.0071}_{-0.0069}/1.9276^{+0.0068}_{-0.0066}$
14	[0.5,0.7]	[-21.5,-21.0]	10118646/6161085	18.1256/11.0364	$0.0221^{+0.0013}_{-0.0011}/0.0212^{+0.0011}_{-0.0009}$	$1.3865^{+0.0343}_{-0.0299}/1.6075^{+0.0331}_{-0.0290}$
15	[0.5,0.7]	[-22.0,-21.5]	5509779/3639334	9.8697/6.5192	$0.0192^{+0.0008}_{-0.0007}/0.0187^{+0.0007}_{-0.0006}$	$1.5620^{+0.0244}_{-0.0224}/1.7465^{+0.0241}_{-0.0220}$
16	[0.5,0.7]	[-23.0,-22.0]	2915483/2002685	5.2225/3.5874	$0.0129^{+0.0002}_{-0.0002}/0.0118^{+0.0002}_{-0.0002}$	$1.7861^{+0.0099}_{-0.0095}/1.9824^{+0.0100}_{-0.0099}$
17	[0.6,0.8]	[-22.0,-21.5]	7093064/4279621	10.4952/6.3323	$0.0230^{+0.0014}_{-0.0012}/0.0232^{+0.0014}_{-0.0012}$	$1.6575^{+0.0424}_{-0.0371}/1.8474^{+0.0471}_{-0.0419}$
18	[0.6,0.8]	[-23.0,-22.0]	3846490/2478615	5.6914/3.6675	$0.0178^{+0.0006}_{-0.0005}/0.0175^{+0.0006}_{-0.0005}$	$1.9046^{+0.0227}_{-0.0213}/2.1385^{+0.0253}_{-0.0234}$
19	[0.7,0.9]	[-23.0,-22.0]	5096945/3130438	6.4861/3.9836	$0.0240^{+0.0014}_{-0.0012}/0.0244^{+0.0015}_{-0.0012}$	$2.0244^{+0.0500}_{-0.0437}/2.3440^{+0.0591}_{-0.0500}$
20	[0.8,1.0]	[-23.0,-22.0]	5854132/3323035	6.6040/3.7487	$0.0261^{+0.0019}_{-0.0016}/0.0243^{+0.0014}_{-0.0012}$	$1.9435^{+0.0616}_{-0.0537}/2.1950^{+0.0551}_{-0.0479}$

mator [88-90],

$$\xi^{\text{obs}}(r_p, r_\pi) = \frac{\text{DD} - 2\text{DR} + \text{RR}}{\text{RR}} \quad (3)$$

where DD, RR and DR are normalized number of galaxy-galaxy, random-random and galaxy-random pairs within the projected separation r_p and the line-of-sight separation r_π , respectively.

We use the public random catalogs (*randoms-inside*⁵) released along with LS DR8 to account for the survey geometry and angular selection function. When making the random catalogs, we adopt the same cut (i.e., require objects to have at least 1 exposure in each optical band, remove low galactic altitude region, and apply same masks) to make sure that random catalog have the same angular selection with the corresponding galaxy sample. Here we use the ‘shuffled’ redshift method to generate the random samples to compensate possible systematic selection effects as a function of redshift

in the observational (sub-)samples. The random catalog for each galaxy (sub-)sample contains ~5 times as many galaxies. We employ the python package *CorrFunc* to compute the pair-counts [91, 92].

We adopt the sample mean from jackknife resampling method as our estimation of projected 2PCF. The covariance matrix is also estimated with the jackknife method. The footprint of the galaxy sample is divided into $N = 120$ spatially contiguous and equal area sub-regions utilizing the python package *kmeans_radec*⁶. We measure w_p for 120 times leaving out one different sub-region at each time, and the covariance is calculated as 119 times the variance of the 120 measurements [36, 38, 40, 49, 57, 93].

5) <https://www.legacysurvey.org/dr8/files/#random-catalogs>

6) https://github.com/esheldon/kmeans_radec

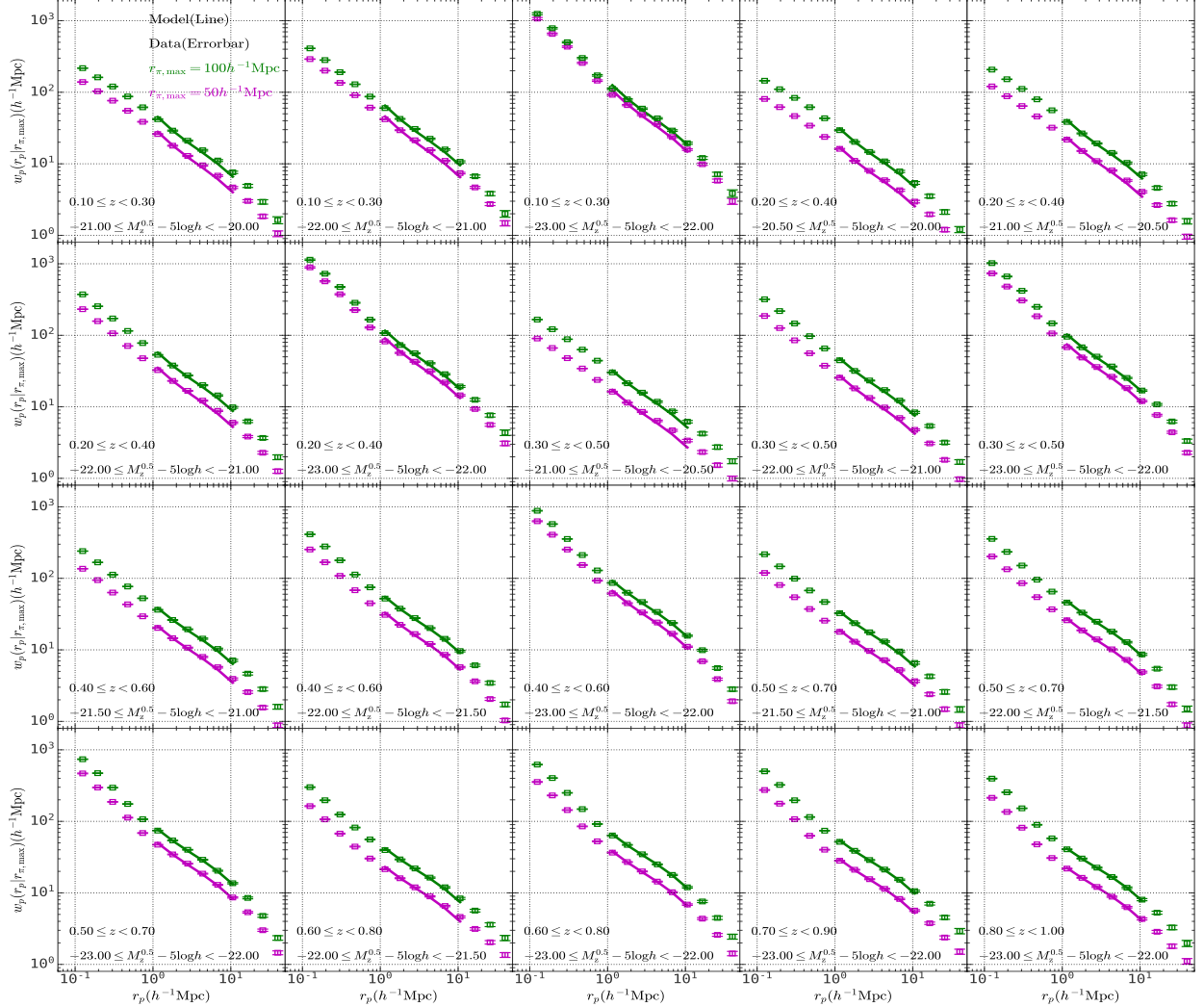


Figure 3 Observational measurements and model predictions of the projected 2PCFs for two different $r_{\pi,\max} = 50$ (100) $h^{-1}\text{Mpc}$ values. We use open squares with errorbars to represent the observational measurements and solid lines to represent the model predictions. Shown in different (in total 20) panels are results for different galaxy samples (as indicated).

3 Methodology

The method and performance tests of our photometric redshift modeling of the 2PCFs were presented in W19 using N-body simulations, here we just briefly summarize the key points.

We model the photometric redshift uncertainty as a Gaussian distribution, which is

$$P(z_{\text{phot}} - z_{\text{spec}}) = \mathcal{N}(0, \sigma_z(1 + z_{\text{spec}})) \quad (4)$$

where z_{phot} is the photometric redshift, z_{spec} is the spectroscopic redshift, $\mathcal{N}(\mu, \sigma)$ is a Gaussian distribution with mean μ and scale σ , and σ_z is the uncertainty of the photometric redshift we want to infer.

To calculate the 2PCF, we need to convert the redshift to

comoving distance, which is

$$D_c(z_{\text{phot}}) = \frac{c}{H_0} \int_0^{z_{\text{phot}}} \frac{dz'}{E(z')} \quad (5)$$

$$\approx D_c(z_{\text{spec}}) + \frac{c(z_{\text{phot}} - z_{\text{spec}})}{H_0 E(z_{\text{spec}})} \quad (6)$$

where $E(z) = \sqrt{\Omega_m(1+z)^3 + \Omega_\Lambda}$. In the 2PCF measurements, we count galaxy pairs as a function of their separations $DD(r_p, r_\pi)$, where $r_\pi = D_c(z_1) - D_c(z_2)$. Because of the photoz error, the probability distribution of the difference between photoz derived separation and spectroscopic redshift derived separation follows,

$$P(R) = \frac{1}{\sqrt{2\pi}\sigma_R} \exp\left(-\frac{R^2}{2\sigma_R^2}\right) \quad (7)$$

$$\sigma_R = \frac{\sqrt{2}c\sigma_z(1 + z_{\text{spec}})}{H_0 E(z_{\text{spec}})} \quad (8)$$

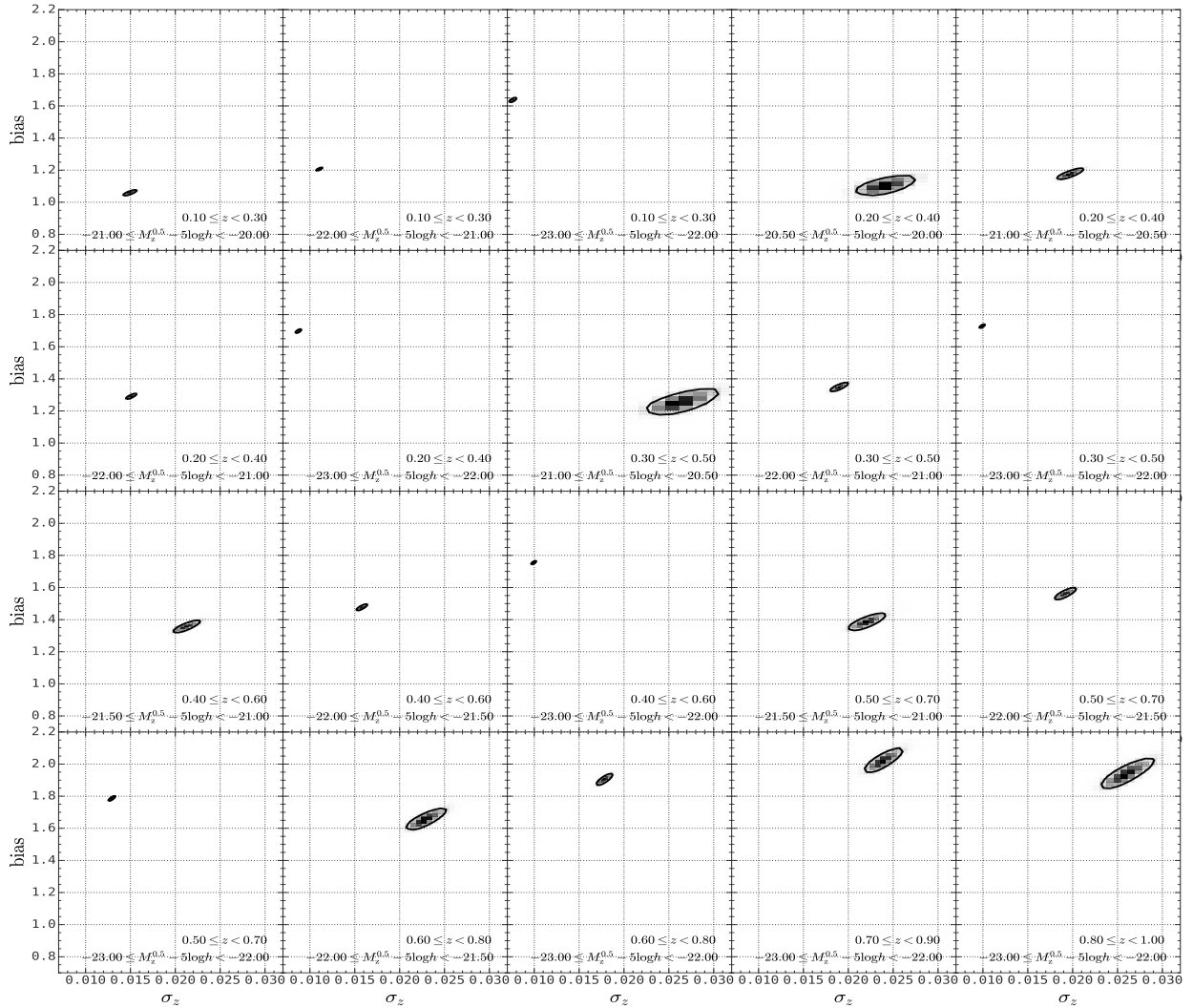


Figure 4 The 2D contours of the parameters σ_z and bias for 20 different all galaxy samples. The black solid contour in each panel corresponds to the 68% confidence region.

where $R \equiv r_\pi(z_{\text{phot}}) - r_\pi(z_{\text{spec}})$.

Theoretically, the 2PCF of galaxies on large scales in redshift space can be described by,

$$\xi^{\text{model}}(r_p, r_\pi) = \int_{-\infty}^{\infty} b^2 \times \xi^{\text{mm}}(r_p, r_\pi - R) P(R) dR \quad (9)$$

where ξ^{mm} is the correlation function of matter calculated from CAMB [94], and b is the galaxy linear bias⁷⁾. The projected 2PCF in the model can also be calculated as

$$w_p^{\text{model}}(r_p | r_{\pi, \text{max}}) = 2 \int_0^{r_{\pi, \text{max}}} \xi^{\text{model}}(r_p, r_\pi) dr_\pi. \quad (10)$$

Here we constrain the two free parameters, σ_z and b , by maximizing the posterior distribution

$$P_{\text{posterior}}(\sigma_z, b) = P_{\text{prior}}(\sigma_z, b) \times \mathcal{L}(\mathcal{D} | \sigma_z, b) \quad (11)$$

where the likelihood is

$$\log \mathcal{L} \propto (\mathbf{w}_p^{\text{obs}} - \mathbf{w}_p^{\text{model}})^T \mathbf{C}^{-1} (\mathbf{w}_p^{\text{obs}} - \mathbf{w}_p^{\text{model}}) \quad (12)$$

where $\mathbf{w}_p^{\text{obs}}$ is the concatenated vector of projected 2PCF integrated to different upper bound, i.e. $\mathbf{w}_p^{\text{obs}} = [\mathbf{w}_p^{\text{obs}}(50h^{-1}\text{Mpc}), \mathbf{w}_p^{\text{obs}}(100h^{-1}\text{Mpc})]$, and \mathbf{C} is the error covariance matrix of the data vector inferred from the jackknife method [39, 58, 95]. The prior distributions for σ_z and b are uniform distribution, and in the range of $[0.0001, 0.5 \times z_{\text{max}}]$ and $[0.01, 10.0]$, respectively, where z_{max} is the maximum redshift in each sample, because σ_z increases as redshift get higher. Here we employed the emcee [96] package to sample the posterior distribution of σ_z and b .

7) More accurate modeling of the galaxy 2PCFs, especially on small one-halo term scales, can be achieved using the HOD/CLF models, which we will present in a subsequent probe.

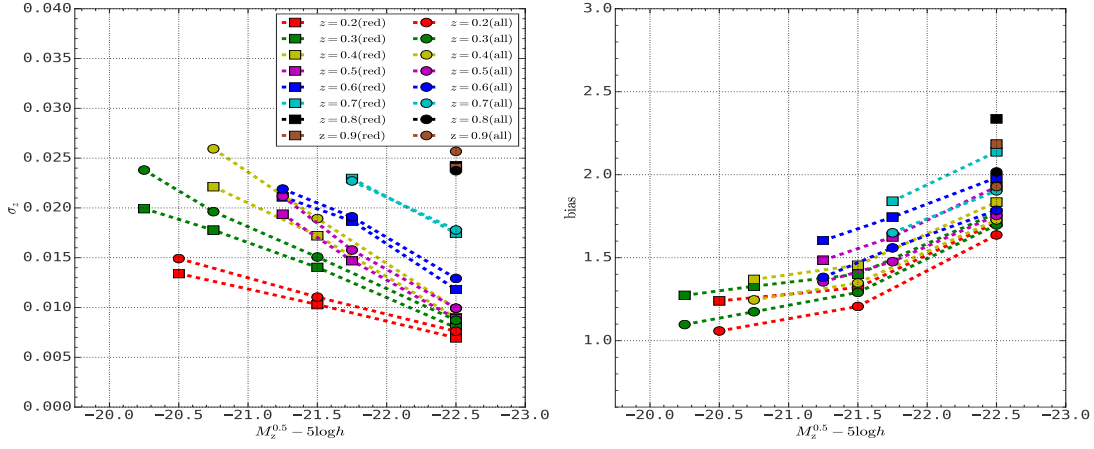


Figure 5 The best fit σ_z and bias measurements for galaxy (sub-)samples in the DESI Imaging Legacy Surveys within different absolute magnitude and redshift bins. Different colors represent galaxy (sub-)samples in different redshifts bins.

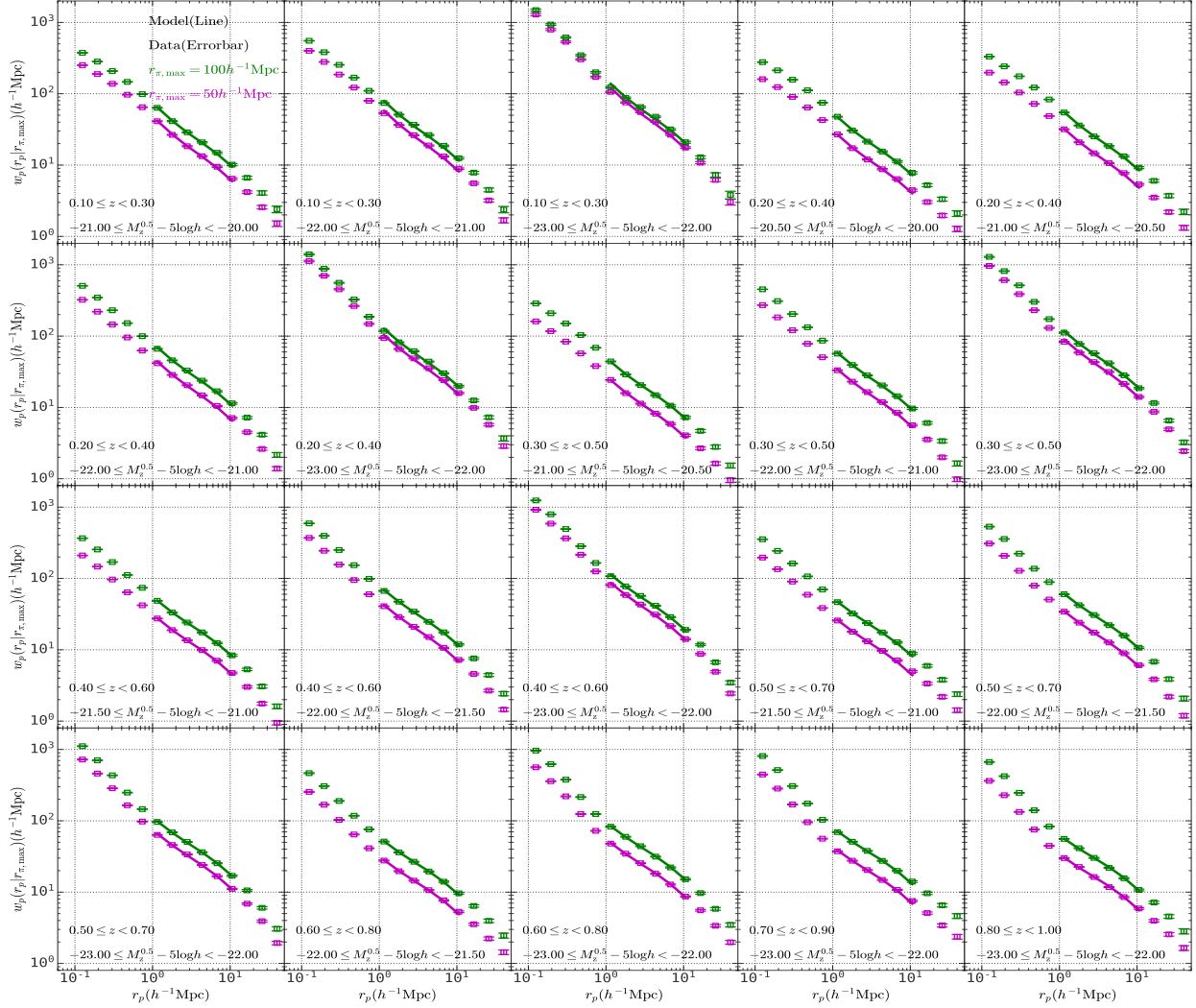


Figure 6 Similar to Fig. 3, but here for 20 red galaxy sub-samples.

4 Results

4.1 Model fitting

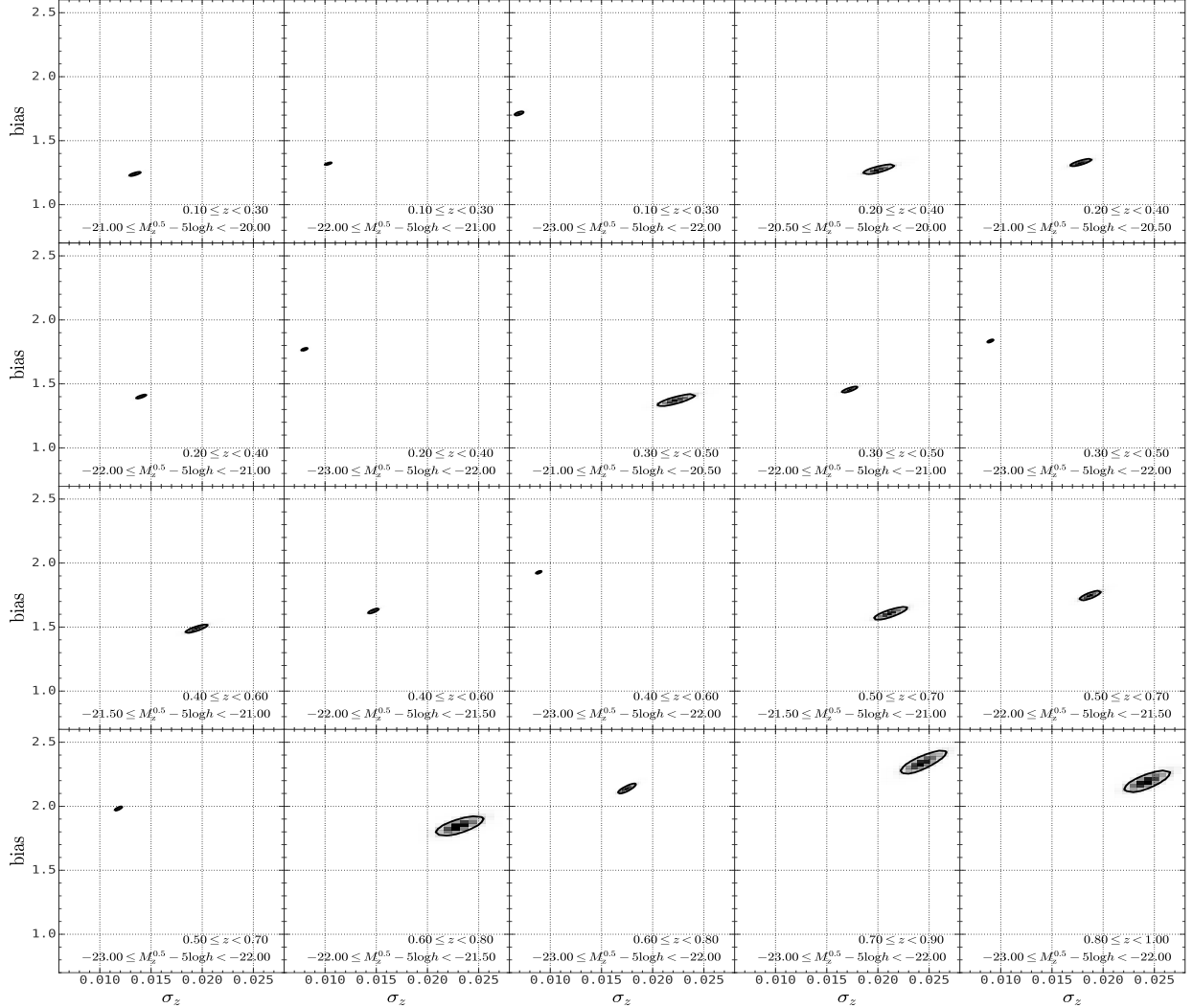


Figure 7 Similar to Fig. 4, but here for 20 red galaxy sub-samples.

We start our investigation with 20 all galaxy samples. In Figure 3, we show w_p^{obs} measurements (open squares) in different redshift and magnitude bins, where r_p is from 10^{-1} to $10^{1.7} h^{-1} \text{Mpc}$ in 15 logarithmic bins. Here results are shown for the projected 2PCFs calculated with two different $r_{\pi,\text{max}} = 50/100 h^{-1} \text{Mpc}$ values. As shown in the figure, galaxies in brighter magnitude bins in general have stronger clustering strengths. While the clustering amplitude differences between two different $r_{\pi,\text{max}}$ become closer as galaxies become brighter or in the lower redshift bins, which indicate relatively smaller σ_z .

Quantitatively, we use $w_p^{\text{obs}}(r_p | r_{\pi,\text{max}})$ on scales from $r_p = 1$ to $10 h^{-1} \text{Mpc}$ to constrain our model parameters, σ_z and b . The reasons of using these scales are two folded: (1) on smaller scales, the galaxy bias becomes nonlinear. (2) on larger scales, the 2PCFs may somehow suffer from the systematic photometric redshift errors.

For each galaxy sample, we run 10 Markov Chain Monte Carlo (MCMC) chains, each with 50,000 steps. The chains converge within the first 10,000 steps mostly, these steps are discarded because they are regarded as burn-in stage. Finally we obtain about 400,000 MCMC models. The posterior distributions of the model parameters are shown in Figure 4. The best-fit σ_z and galaxy bias are listed in Table 1. We show in Fig. 3 using solid lines the best fitting model predictions. Overall, our model can accurately recover the clustering signals in different redshift and luminosity bins.

Looking into the best fitting parameters themselves, as shown in the left panel of Figure 5 using open circles, we found the photoz errors get larger when galaxies become fainter and locate at larger redshifts. Quite interestingly, our model constraints on this value are in nice agreement with the direct measurements of the photoz errors from a small sample of galaxies that have spectroscopic redshifts [81]. The

open circles shown in the right panel of Figure 5 are the best fit galaxy biases in different absolute magnitude and redshift bins. Obviously, galaxy biases become larger when galaxies are brighter and locate at higher redshifts. For the brightest galaxy samples, the bias increase from ~ 1.6 at $z \sim 0.2$ to ~ 2.0 at $z \sim 0.8$.

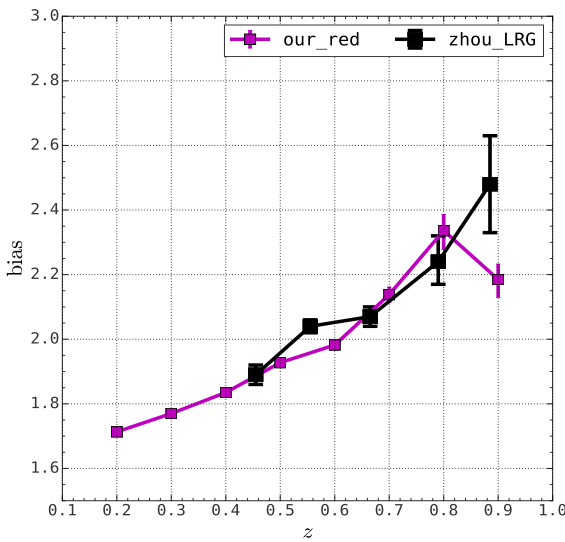


Figure 8 Our best fit bias measurements for the brightest red galaxy sub-samples in the DESI Imaging Legacy Surveys compared with the bias measurements from luminous red galaxy (LRG) samples obtained by [81] as a function of redshift.

Next, we turn to the 20 red galaxy sub-samples. Similar to the 20 all galaxy samples, we also measure their w_p^{obs} with two different $r_{\pi,\text{max}} = 50/100 h^{-1}\text{Mpc}$ values. The results are shown in Fig. 6 using open squares. The overall behaviors are quite similar to those of all galaxy samples. Here we can see that the gap between w_p^{obs} for different $r_{\pi,\text{max}}$ values become even smaller in these red sub-samples.

Following the same procedures for each of the 20 all galaxy samples, we run 10 MCMC chains, each with 50,000 steps for each of our red galaxy subsamples. After discarding the burn-in stage models, we use the remaining 400,000 MCMC models to describe the posterior distributions of the model parameters. The results are shown in Fig. 7 with contours. We also list the best-fit σ_z and galaxy bias for our 20 red galaxy subsamples in Table 1. As an illustration, we show in Fig. 6 using solid lines the best fitting model predictions. Here again, our models accurately recover the clustering signals in different redshift and luminosity bins.

In addition to the red galaxy sub-samples, we also looked into the 20 blue galaxy sub-samples. However, as we will demonstrate in the Appendix, the blue sub-samples might suffer from systematic photometric redshift uncertainties,

where their clustering measurements can not be well modelled.

Because of these, we only focus on the red and all galaxy (sub-)samples to model their color dependence. As shown in the Fig. 5, red galaxy sub-samples show smaller σ_z and higher galaxy bias in the same redshift and absolute magnitude bins. The difference is larger in less bright galaxy (sub-)samples.

Finally, we compare our bias measurements with the ones obtained in a recent similar study [81] in Fig. 8. The black squares with error bars shown in this figure are the bias measurements obtained by Zhou et al. [81] from the DECaLS DR7 using an HOD fitting algorithm, while our results are shown as the magenta squares. In that study, they also used the projected 2PCFs measured from the photometric redshift data and made their model constraints. However, unlike our two integration depths method, they treat photoz error as a prior to assign a redshift error to each galaxy in their mock samples. By comparing the observed 2PCFs with the mock 2PCFs they fitted the related HOD model parameters, and hence obtained the biases of galaxies. To have fair comparisons with their luminous red galaxy (LRG) samples, we only show our best fit bias measurements for the brightest red galaxy sub-samples. Taking into account the different galaxy number densities between the two sets of galaxy samples, overall, our results agree with their measurements quite well at redshift $z > 0.6$. Indeed the discrepancy in the highest redshift bin is mainly induced by the galaxy selection where their galaxy number density in that bin is much lower than ours. On the other hand, their biases measured from the two lower redshift bins are somewhat larger than ours. We argue that this might be caused by a bit too large assigned photoz errors in their modelling. Note that our measurements and model constraints show that photoz errors decrease significantly at lower redshifts.

4.2 The intrinsic projected 2PCFs

After we modeled the projected 2PCFs to different $r_{\pi,\text{max}}$ using the σ_z and bias parameters, we can in general get an estimate of their intrinsic values, i.e. the projected 2PCFs in real space, which corresponds to $w_p^{\text{obs}}(r_p) = w_p^{\text{obs}}(r_p|r_{\pi,\text{max}} = \infty)$ here. This set of measurements are very important for galaxy formation and cosmological constraints in the HOD modelings. We use the following equation to estimate the observational intrinsic projected 2PCFs,

$$w_p^{\text{obs}}(r_p) = w_p^{\text{obs}}(r_p|r_{\pi,\text{max}}) * w_p^{\text{model}}(r_p)/w_p^{\text{model}}(r_p|r_{\pi,\text{max}}), \quad (13)$$

where we use $r_{\pi,\text{max}} = 100 h^{-1}\text{Mpc}$ cut to make the estimation. Note that this equation holds accurately if the observed

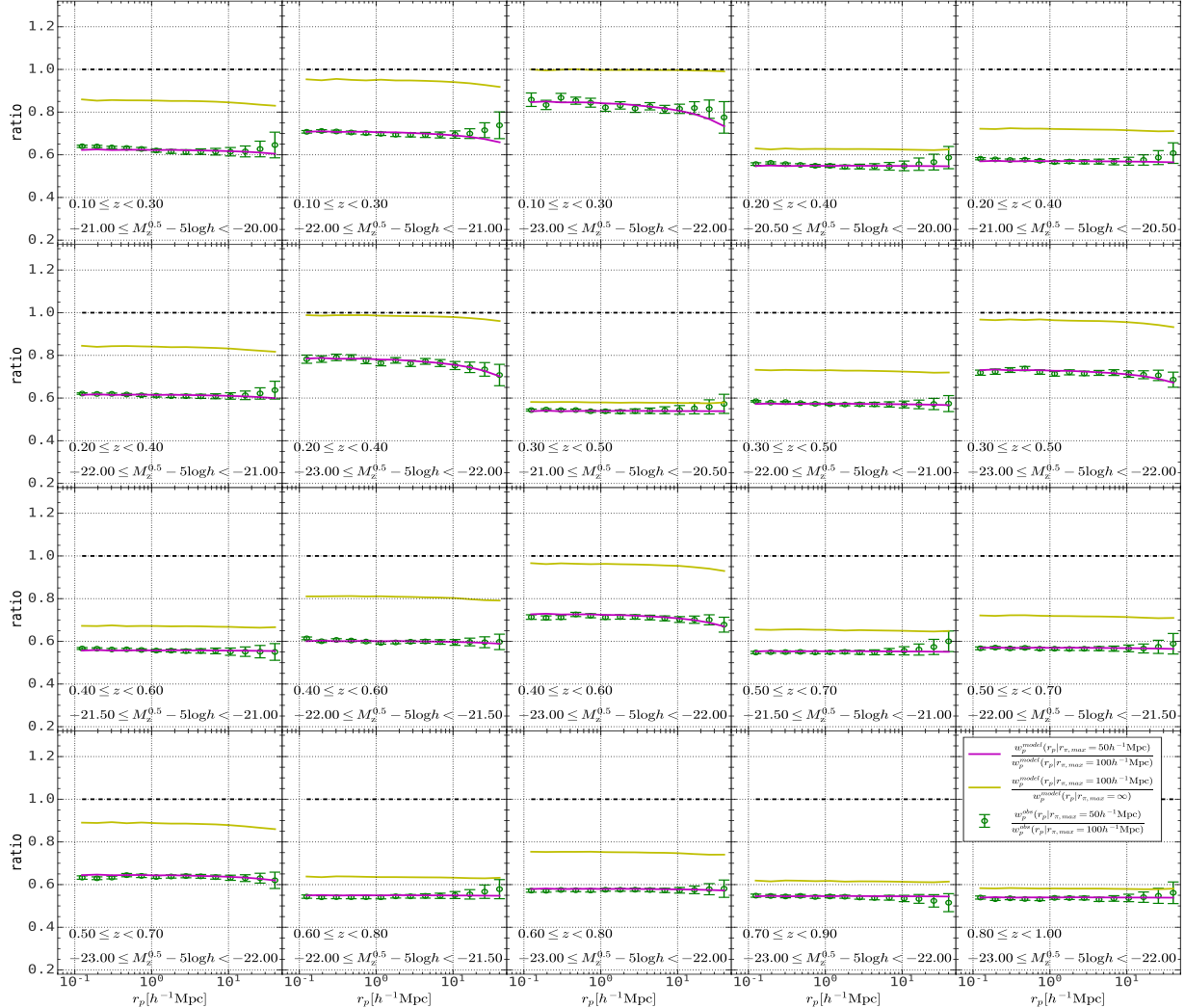


Figure 9 The ratio of projected 2PCFs. The purple lines and open circles with error-bars are results for the model $w_p^{\text{model}}(r_p|r_{\pi,\text{max}})$ ratios and the observed $w_p^{\text{obs}}(r_p|r_{\pi,\text{max}})$ ratios for the two $r_{\pi,\text{max}} = 50$ and $100 h^{-1}\text{Mpc}$ cuts, respectively. The yellow solid lines are model predictions of $w_p^{\text{model}}(r_p|r_{\pi,\text{max}})/w_p^{\text{model}}(r_p)$ for $r_{\pi,\text{max}} = 100 h^{-1}\text{Mpc}$ cut.

2PCFs are related with the dark matter 2PCF by a constant bias factor. Unless the bias factor has a very strong scale dependence, especially on small scales, the correction factor $w_p^{\text{model}}(r_p)/w_p^{\text{model}}(r_p|r_{\pi,\text{max}})$ may be slightly different for the observed galaxies.

To test the reliability and assess the accuracy of using the model $w_p^{\text{model}}(r_p)/w_p^{\text{model}}(r_p|r_{\pi,\text{max}})$ ratio based on the auto-correlation function of dark matter particles to account for that of galaxies, we show in Fig. 9 for 20 all galaxy samples a comparison of the model $w_p^{\text{model}}(r_p|r_{\pi,\text{max}})$ ratios and the observed $w_p^{\text{obs}}(r_p|r_{\pi,\text{max}})$ ratios for the two $r_{\pi,\text{max}} = 50$ and $100 h^{-1}\text{Mpc}$ cuts, respectively. The open circles with error-bars shown in Fig. 9 are the results for the observed $w_p^{\text{obs}}(r_p|r_{\pi,\text{max}})$ ratios, which show very weak scale dependence. The purple solid lines are the results for the model $w_p^{\text{model}}(r_p|r_{\pi,\text{max}})$ ratios. Note that although our model parameters are only con-

strained using the $w_p^{\text{obs}}(r_p|r_{\pi,\text{max}})$ values on scales between $r_p = 1$ and $10 h^{-1}\text{Mpc}$, overall, the predicted model ratios agree with the observed ratios very well, i.e., within $1-\sigma$ error-bars on all the scales. Next, the model predictions of $w_p^{\text{model}}(r_p|r_{\pi,\text{max}})/w_p^{\text{model}}(r_p)$ for $r_{\pi,\text{max}} = 100 h^{-1}\text{Mpc}$ cut are shown in Fig. 9 using yellow solid lines. In all the cases, we find that this set of correction factors are all larger (i.e., less significant) than those between $r_{\pi,\text{max}} = 50$ and $100 h^{-1}\text{Mpc}$ cuts. And the scale dependence is also weaker. Based on these features, we infer that the overall correction in Eq. 13 is reliable and the errors induced in this step should not exceed $1-\sigma$ errors of the observational data. To be conservative, we will enlarge the error-bars in our extracted intrinsic projected 2PCFs by a factor of two for future use. We also checked the situation for the 20 red galaxy sub-samples, for simplicity not explicitly shown here, the overall behaviors are quite similar

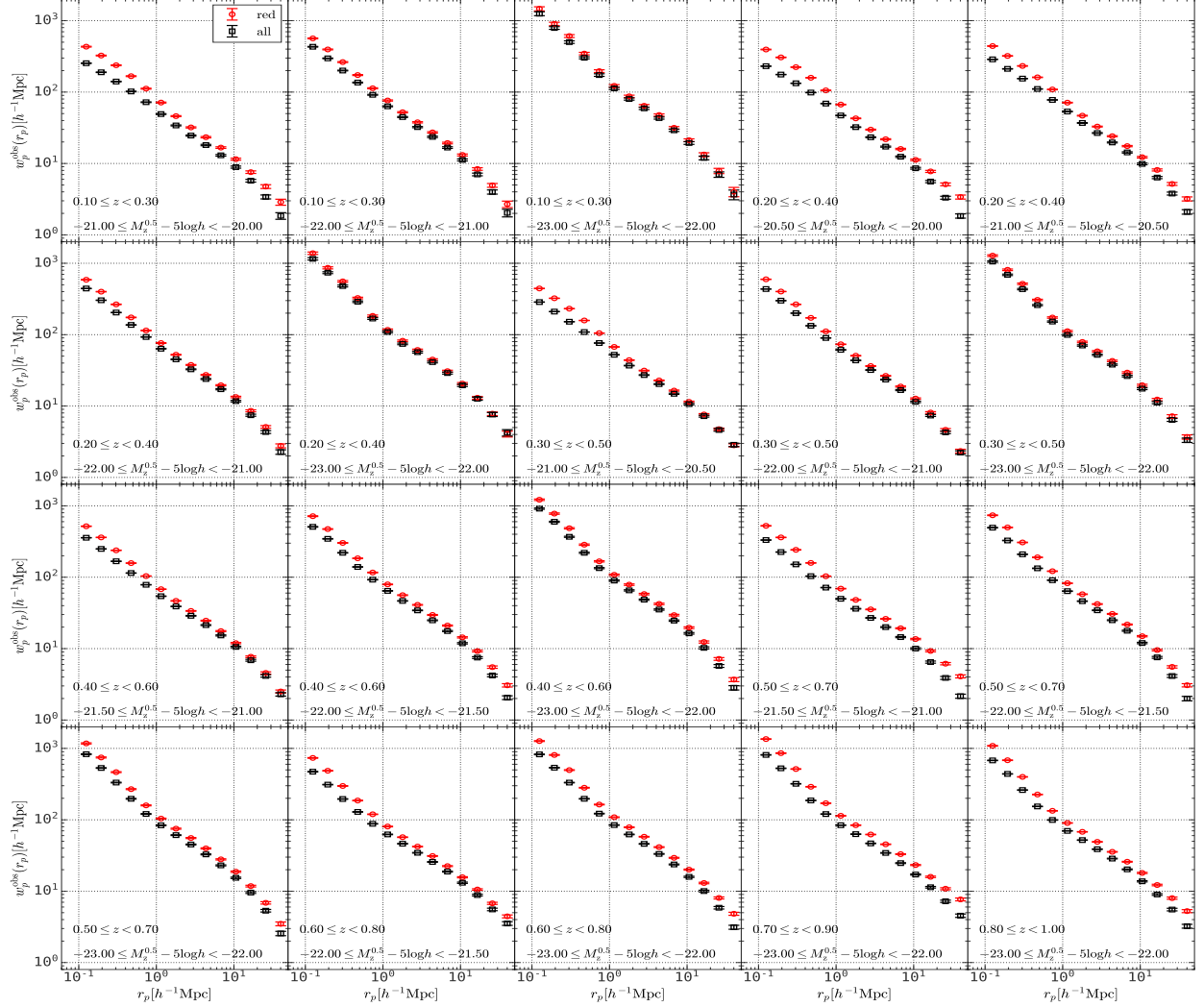


Figure 10 The extracted intrinsic projected 2PCFs for all and red galaxy (sub-)samples. Here the error-bars in each (sub-)sample are enlarged by a factor of 2 with respect to the direct measurements in $w_p^{\text{obs}}(r_p|r_{\pi,\text{max}})$ with $r_{\pi,\text{max}} = 100 h^{-1} \text{Mpc}$ cut.

to the 20 all galaxy samples.

Shown in Fig. 10 are the intrinsic projected 2PCFs we obtained for the all and red galaxy (sub-)samples. As we mentioned, here the error-bars in each (sub-)sample are enlarged by a factor of 2 with respect to the direct measurements in $w_p^{\text{obs}}(r_p|r_{\pi,\text{max}})$ with $r_{\pi,\text{max}} = 100 h^{-1} \text{Mpc}$ cut. We can see that overall, in the same redshift and luminosity bin, the red galaxies show somewhat stronger clustering strength than the all galaxies. The projected 2PCFs on small scales is more enhanced in red sub-samples than the all samples. These features in general hold important information regarding how galaxies with different colors populated dark matter halos and the related galaxy formation and evolution processes. We will come to this topic in subsequent probes.

5 Summary

In this study, we construct 60 volume-limited galaxy (sub-)samples, sampling 8 redshift bins from $z = 0.1$ to $z = 1.0$, and a few z-band absolute magnitude bins with $M_z \leq -20$, from the photometric redshift galaxy catalogs of the DESI Imaging Legacy Surveys DR8. We measure the projected 2PCFs for all these 60 (sub-)samples with two $r_{\pi,\text{max}} = 50$ and $100 h^{-1} \text{Mpc}$ cuts along the line-of-sight directions, respectively. Using the photometric redshift modeling of the 2PCFs developed in W19, we constrain the photoz errors and galaxy biases for all the 60 volume-limited galaxy (sub-)samples. Our main results are summarized as follows.

- Our model can well describe the clustering properties of the red and all galaxy (sub-)samples, while the blue galaxy sub-samples might suffer from the systematic redshift errors, especially for low redshift bins, where the clustering on large

scales are significantly enhanced and can not be described by the theoretical models.

- Focusing only on the 40 red and all galaxy (sub-)samples, we find galaxies show better photoz performance and have higher biases when they become redder, brighter or in a lower redshift bin.
- Based on the projected 2PCFs for the $r_{\pi,\max} = 100 h^{-1}\text{Mpc}$ cut, and the theoretical model prediction of the correction factor, we obtain the intrinsic projected 2PCFs for 40 red and all galaxy (sub-)samples.

Here we note that we did not take photoz redshift outliers into account, which according to [81] are at less than 1% level. And we assumed that the photometric redshift errors follow Gaussian distribution which is also quite well demonstrated in [81]. With the intrinsic clustering measurements for 40 red and all galaxy (sub-)samples, we will go deep into HOD/CLF framework to explore the halo-galaxy connection in a subsequent probe.

This work is supported by the national science foundation of China (grant Nos. 11833005, 11890691, 11890692, 11533006, 11621303), Shanghai Natural Science Foundation, Grant No. 15ZR1446700 and 111 project No. B20019. The Photometric Redshifts for the Legacy Surveys (PRLS) catalog used in this paper was produced thanks to funding from the U.S. Department of Energy Office of Science, Office of High Energy Physics via grant DE-SC0007914.

Conflict of interest The authors declare that they have no conflict of interest.

- Shectman, S. A., Landy, S. D., Oemler, A., et al. *ApJ*, 470, 172 (1996).
- Colless, M., Dalton, G., Maddox, S., et al. *MNRAS*, 328, 1039 (2001).
- York, D. G., Adelman, J., Anderson, Jr., J. E., et al. *AJ*, 120, 1579 (2000).
- Coil, A. L., Davis, M., Madgwick, D. S., et al. *ApJ*, 609, 525 (2004).
- Coil, A. L., Newman, J. A., Croton, D., et al. *ApJ*, 672, 153 (2008).
- Guzzo, L., Scoggio, M., Garilli, B., et al. *A&A*, 566, A108 (2014).
- Bassett, B., & Hlozek, R. Baryon acoustic oscillations, 246 (2010).
- Padmanabhan, N., Xu, X., Eisenstein, D. J., et al. *MNRAS*, 427, 2132 (2012).
- Anderson, L., Aubourg, J., Bailey, S., et al. *MNRAS*, 441, 24 (2014).
- Aubourg, J., Bailey, S., Bautista, J. E., et al. *PhRvD*, 92, 123516 (2015).
- Sarpa, E., Schimd, C., Branchini, E., & Matarrese, S. *MNRAS*, 484, 3818 (2019).
- Bartelmann, M., & Schneider, P. *PhR*, 340, 291 (2001).
- Hoekstra, H., & Jain, B. Annual Review of Nuclear and Particle Science, 58, 99 (2008).
- Vegetti, S., Koopmans, L. V. E., Auger, M. W., Treu, T., & Bolton, A. S. *MNRAS*, 442, 2017 (2014).
- Han, J., Eke, V. R., Frenk, C. S., et al. *MNRAS*, 446, 1356 (2015).
- Wang, W., White, S. D. M., Mandelbaum, R., et al. *MNRAS*, 456, 2301 (2016).
- Zhang, J., Luo, W., & Foucaud, S. *JCAP*, 2015, 024 (2015).
- Luo, W., Yang, X., Zhang, J., et al. *ApJ*, 836, 38 (2017).
- Luo, W., Yang, X., Lu, T., et al. *ApJ*, 862, 4 (2018).
- Dong, F., Zhang, J., Yu, Y., et al. *ApJ*, 874, 7 (2019).
- Feldman, H. A., Kaiser, N., & Peacock, J. A. *ApJ*, 426, 23 (1994).
- Hamilton, A. J. S., & Tegmark, M. *MNRAS*, 330, 506 (2002).
- Tegmark, M., Hamilton, A. J. S., & Xu, Y. *MNRAS*, 335, 887 (2002).
- Tegmark, M., Blanton, M. R., Strauss, M. A., et al. *ApJ*, 606, 702 (2004).
- Beutler, F., Blake, C., Colless, M., et al. *MNRAS*, 416, 3017 (2011).
- Li, Z., Jing, Y. P., Zhang, P., & Cheng, D. *ApJ*, 833, 287 (2016).
- Percival, W. J., Baugh, C. M., Bland-Hawthorn, J., et al. *MNRAS*, 327, 1297 (2001).
- Percival, W. J., Cole, S., Eisenstein, D. J., et al. *MNRAS*, 381, 1053 (2007).
- Percival, W. J., Reid, B. A., Eisenstein, D. J., et al. *MNRAS*, 401, 2148 (2010).
- Gaztaaga, E., & Scoccimarro, R. *MNRAS*, 361, 824 (2005).
- Guo, H., Jing, Y. P. *ApJ*, 698, 479 (2005).
- Guo, H., Jing, Y. P. *ApJ*, 702, 425 (2009).
- Jing, Y. P., Mo, H. J., Brner, G. *ApJ*, 494, 1 (1998).
- Yang, X., Mo, H. J., Jing, Y. P., van den Bosch, F. C., Chu, Y. *MNRAS*, 350, 1153 (2004).
- Eisenstein, D. J., Zehavi, I., Hogg, D. W., et al. *ApJ*, 633, 560 (2005).
- Zehavi, I., et al. *ApJ*, 630, 1 (2005).
- Li, C., Kauffmann, G., Jing, Y. P., et al. *MNRAS*, 368, 21 (2006).
- Zehavi, I., Zheng, Z., Weinberg, D. H., et al. *ApJ*, 736, 59 (2011).
- Guo, H., Zheng, Z., Zehavi, I., et al. *MNRAS*, 441, 2398 (2014).
- Guo, H., Zheng, Z., Zehavi, I., et al. *MNRAS*, 453, 4368 (2015).
- Shi, F., Yang, X., Wang, H., et al. *ApJ*, 833, 241 (2016).
- Guo, H., Yang, X., Lu, Y. *ApJ*, 858, 30 (2018).
- Xu, H., Zheng, Z., Guo, H., et al. *MNRAS*, 481, 5470 (2018).
- Berlind, A. A., Weinberg, D. H. *ApJ*, 575, 587 (2002).
- Zheng, Z., Berlind, A. A., Weinberg, D. H., et al. *ApJ*, 633, 791 (2005).
- Guo, H., Zheng, Z., Behroozi, P. S., et al. *MNRAS*, 459, 3040 (2016).
- Yuan, S., Eisenstein, D. J., Garrison, L. H. *MNRAS*, 478, 2019 (2018).
- Zu, Y., Mandelbaum, R. *MNRAS*, 454, 1161 (2015).
- Zu, Y., Mandelbaum, R. *MNRAS*, 457, 4360 (2016).
- Zu, Y., Mandelbaum, R. *MNRAS*, 476, 1637 (2018).
- Yang, X., Mo, H. J., van den Bosch, F. C. *MNRAS*, 339, 1057 (2003).
- Cooray, A. *MNRAS*, 365, 842 (2006).
- van den Bosch, F. C., Yang, X., Mo, H. J., et al. *MNRAS*, 376, 841 (2007).
- Yang, X., Mo, H. J., van den Bosch, F. C., Zhang, Y., Han, J. *ApJ*, 752, 41 (2012).
- Rodrguez-Puebla, A., Avila-Reese, V., Yang, X., et al. *ApJ*, 799, 130 (2015).
- Conroy, C., Wechsler, R. H., Kravtsov, A. V. *ApJ*, 647, 201 (2006).
- Xu, H., Zheng, Z., Guo, H., Zhu, J., Zehavi, I. *MNRAS*, 460, 3647 (2016).
- Guo, H., Zehavi, I., Zheng, Z., et al. *ApJ*, 767, 122 (2013).
- Zheng, Z., Coil, A. L., Zehavi, I. *ApJ*, 667, 760 (2007).
- Cacciato, M., van den Bosch, F. C., More, S., et al. *MNRAS*, 394, 929 (2009).
- Cacciato, M., van den Bosch, F. C., More, S., Mo, H., Yang, X. *MNRAS*, 430, 767 (2013).
- Lilly, S. J., Le Fvre, O., Renzini, A., et al. *ApJS*, 172, 70 (2007).
- Masjedi, M., Hogg, D. W., Cool, R. J., et al. *ApJ*, 644, 54 (2006).
- Myers, A. D., White, M., Ball, N. M. *MNRAS*, 399, 2279 (2009).
- Hickox, R. C., Myers, A. D., Brodin, M., et al. *ApJ*, 731, 117 (2011).
- Wang, W., Jing, Y. P., Li, C., Okumura, T., Han, J. *ApJ*, 734, 88 (2011).
- Coupon, J., Kilbinger, M., McCracken, H. J., et al. *A&A*, 542, A5 (2012).
- Harikane, Y., Ouchi, M., Ono, Y., et al. *ApJ*, 821, 123 (2016).
- Harikane, Y., Ouchi, M., Ono, Y., et al. Publications of the Astronomical Society of Japan, 70, S11 (2018).
- He, W., Akiyama, M., Bosch, J., et al. Publications of the Astronomical Society of Japan, 70, S33 (2018).
- Wang, Z., Xu, H., Yang, X., et al. 2019, *ApJ*, 879, 71 (2019).
- Eisenstein, D. J. *ApJ*, 586, 718 (2003).
- Planck Collaboration, Aghanim, N., Akrami, Y., et al. *A&A*, 641, A6 (2020)

- 74 Yang, X., Xu, H., He, M., et al. arXiv e-prints, arXiv:2012.14998 (2020)
- 75 DESI Collaboration, Aghamousa, A., Aguilar, J., et al. ArXiv e-prints, arXiv:1611.00036 (2016)
- 76 Dey, A., Schlegel, D. J., Lang, D., et al. ArXiv e-prints, arXiv:1804.08657 (2018).
- 77 Lang, D., Hogg, D. W., Mykytyn, D. The Tractor: Probabilistic astronomical source detection and measurement ascl:1604.008 (2016)
- 78 Blum, R. D., Burleigh, K., Dey, A., et al. American Astronomical Society Meeting Abstracts 228, 317.01 (2016).
- 79 Zou, H., Zhou, X., Fan, X., et al. PASP, 129, 064101 (2017).
- 80 Silva, D. R., Blum, R. D., Allen, L., et al. American Astronomical Society Meeting Abstracts 228, 317.02 (2016).
- 81 Zhou, R., Newman, J. A., Mao, Y.-Y., et al. arXiv e-prints, arXiv:2001.06018 (2020).
- 82 Zehavi, I., Blanton, M. R., Frieman, J. A., et al. ApJ, 571, 172 (2002)
- 83 Blanton, M. R., Eisenstein, D., Hogg, D. W., Schlegel, D. J., Brinkmann, J. ApJ, 629, 143 (2005)
- 84 Breiman, L. Machine Learning, 45, 5 (2001).
- 85 Huchra, J. P., Macri, L. M., Masters, K. L., et al. ApJS, 199, 26 (2012)
- 86 Jones, D. H., Read, M. A., Saunders, W., et al. MNRAS, 399, 683 (2009)
- 87 Blanton, M. R., Roweis, S. AJ, 133, 734 (2007)
- 88 Landy, S. D., Szalay, A. S. ApJ, 412, 64 (1993).
- 89 Szapudi, I., Szalay, A. S. ApJ, 494, L41 (1998).
- 90 Kerscher, M., Szapudi, I., Szalay, A. S. ApJL, 535, L13 (2000).
- 91 Sinha, M., Garrison, L. Software Challenges to Exascale Computing, ed. A. Majumdar R. Arora (Singapore: Springer Singapore), 30. (2019).
- 92 Sinha, M., Garrison, L. H. MNRAS, 491, 3022 (2020).
- 93 Guo, H., Li, C., Zheng, Z., et al. ApJ, 846, 61 (2017)
- 94 Lewis, A., Challinor, A., Lasenby, A. ApJ, 538, 473 (2000).
- 95 Norberg, P., Baugh, C. M., Gaztaaga, E., Croton, D. J. MNRAS, 396, 19 (2009).
- 96 Foreman-Mackey, D., Hogg, D. W., Lang, D., Goodman, J. PASP, 125, 306 (2013).
- 97 Beck, R., Dobos, L., Budavari, T., Szalay, A. S., Csabai, I. MNRAS, 460, 1371 (2016).
- 98 Zou, H., Gao, J., Zhou, X., Kong, X. ApJS, 242, 8 (2019).
- 99 Marulli, F., Bolzonella, M., Branchini, E., et al. A&A, 557, A17 (2013).
- 100 Cowley, W. I., Caputi, K. I., Deshmukh, S., et al. ApJ, 853, 69 (2018).
- 101 Moutard, T., Arnouts, S., Ilbert, O., et al. A&A, 590, A102 (2016).
- 102 Zheng, Z., Guo, H. MNRAS, 458, 4015 (2016).

Appendix

A1 Results for blue sub-samples

Similar to those clustering measurements and model fittings carried out for the 40 all and red galaxy (sub-)samples in section 4.1, we also looked into the 20 blue galaxy sub-samples. Similar to the 20 all galaxy samples, we also measure their w_p^{obs} with two different $r_{\pi,\text{max}} = 50/100 h^{-1} \text{Mpc}$ values, where the results are shown in Fig. A11 with open squares. The overall behaviors are roughly similar to those of all galaxy samples. Here we can see that the gap between w_p^{obs} for different $r_{\pi,\text{max}}$ values are larger in these blue sub-samples. In addition, we find in a few sub-samples, the projected 2PCFs on large scales are significantly boosted.

Following the same procedures for each of the 20 all galaxy samples, we run 10 MCMC chains, each with 50,000 steps for each of our blue galaxy sub-samples. After discarding the burn-in stage models, we use the remaining 400,000 MCMC models to describe the posterior distributions of the model parameters. The results are shown in Fig. A12 with contours. Here again, we show in Fig. A11 using solid lines the best fitting model predictions. Unlike the 40 all and red (sub-)samples, here we can see that there are some blue sub-samples where our models can not describe their behaviors well, especially those with boosted clustering strengths on large scales. For these sub-samples, our constraints on the photoz error and bias parameters are also quite poor.

Note that even in the framework of a more sophisticated HOD model, the parameters in general can change the shape of w_p on small scales and the amplitude on large scales. Since the clustering of galaxies on large scales is modelled through the combination of a constant galaxy bias and the auto correlation of dark matter particles, the very different shape of w_p on scales $r_p > 3 h^{-1} \text{Mpc}$ shown in Fig. A11 will not be well modelled in the HOD models. We thus believe that there should be some systematic photoz errors or photometry errors in these blue sub-samples, so that their projected 2PCFs on large scales are boosted and can not be well modelled by theory. Because of these, we omit further analysis for these 20 blue galaxy (sub-)samples in this study.

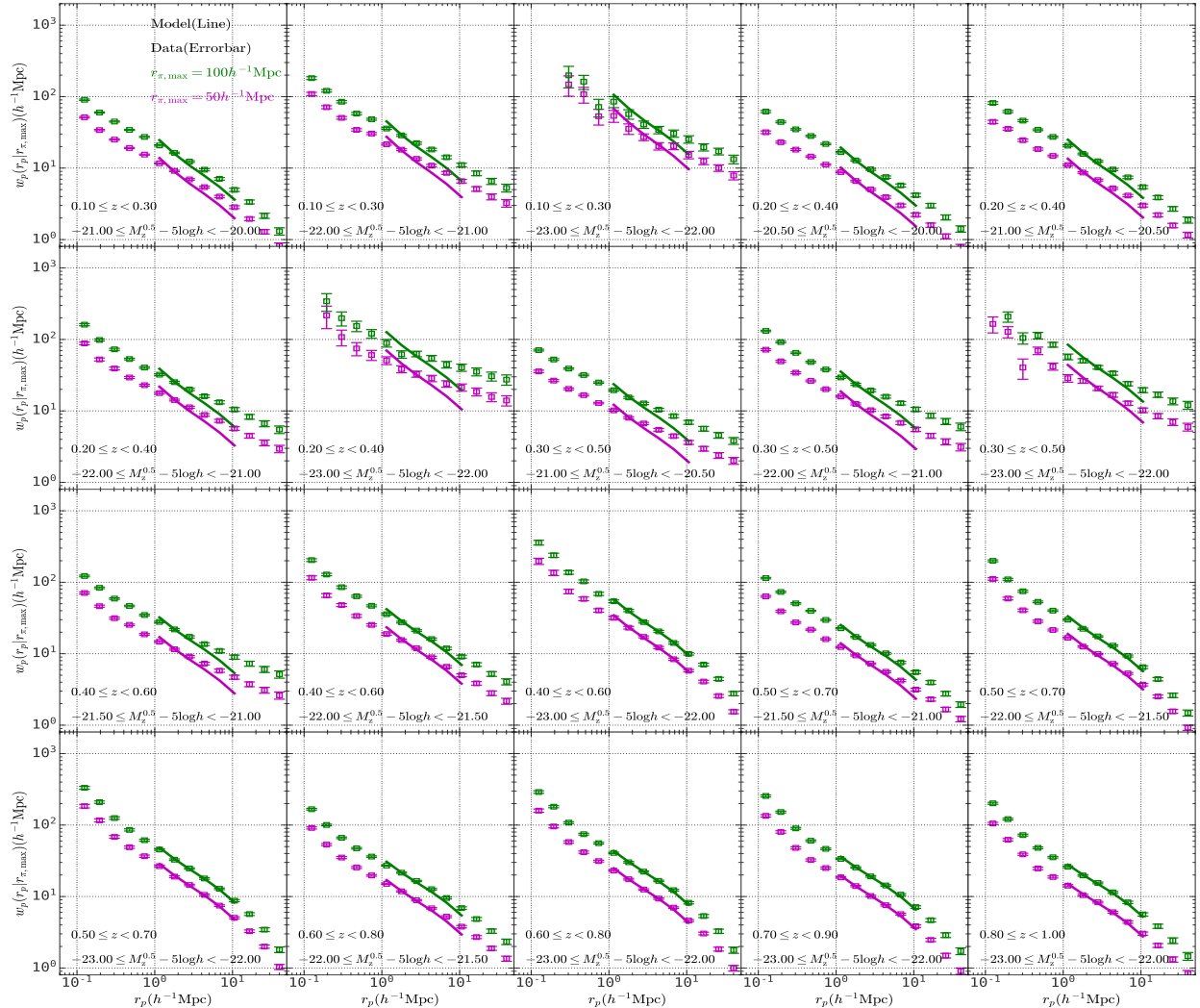


Figure A11 Similar to Fig. 3, but here for 20 blue galaxy sub-samples.

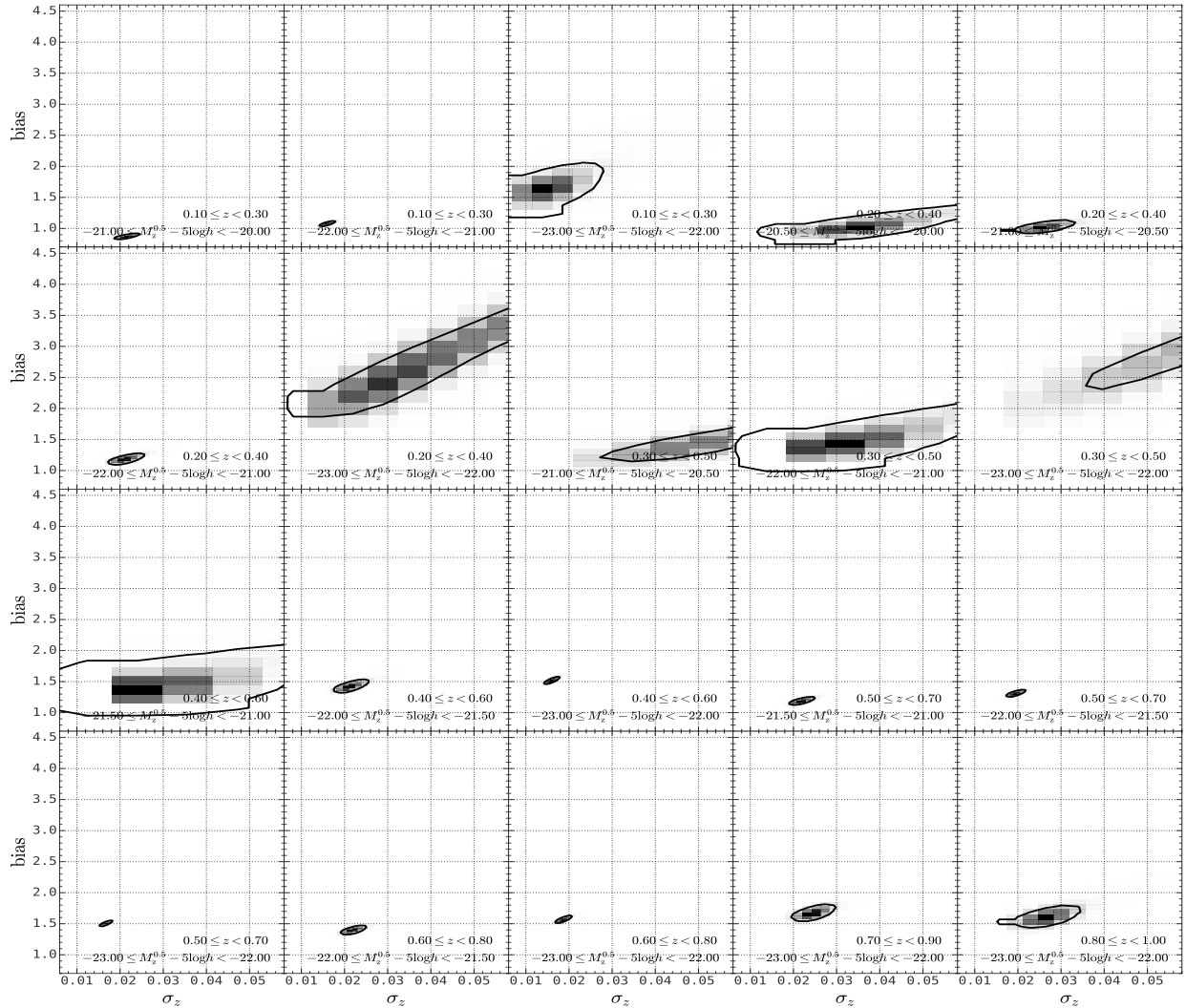


Figure A12 Similar to Fig. 4, but here for 20 blue galaxy sub-samples.